

The POINT-AGAPE Survey I: The Variable Stars in M31. [★]

Jin H. An,^{1†} N. W. Evans,¹ P. Hewett,¹ P. Baillon,² S. Calchi Novati,³ B. J. Carr,⁴
M. Crézé,^{5,6} Y. Giraud-Héraud,⁶ A. Gould,⁷ Ph. Jetzer,³ J. Kaplan,⁶ E. Kerins,⁸
S. Paulin-Henriksson,⁶ S. J. Smartt,¹ C. S. Stalin,⁶ and Y. Tsapras.⁴

(The POINT-AGAPE[‡] collaboration)

¹*Institute of Astronomy, University of Cambridge, Madingley Road, Cambridge CB3 0HA, UK*

²*European Organization for Nuclear Research CERN, CH-1211 Genève 23, Switzerland*

³*Institut für Theoretische Physik, Universität Zürich, Winterthurerstrasse 190, CH-8057 Zürich, Switzerland*

⁴*Astronomy Unit, School of Mathematical Sciences, Queen Mary, University of London, Mile End Road, London E1 4NS, UK*

⁵*Université Bretagne-Sud, Campus de Tohannic, BP 573, F-56017 Vannes Cedex, France*

⁶*Laboratoire de Physique Corpusculaire et Cosmologie, Collège de France, 11 Place Marcelin Berthelot, F-75231 Paris, France*

⁷*Department of Astronomy, Ohio State University, 140 West 18th Avenue, Columbus, OH 43210, USA*

⁸*Astrophysics Research Institute, Liverpool John Moores University, 12 Quays House, Egerton Wharf, Birkenhead CH41 1LD, UK*

Accepted 2004 March 3; Revised version submitted 2004 February 22 (v3), & February 9 (v2); Original version submitted 2004 January 19 (v1)

ABSTRACT

For the purposes of identifying microlensing events, the POINT-AGAPE collaboration has been monitoring the Andromeda galaxy (M31) for three seasons (1999–2001) with the Wide Field Camera on the Isaac Newton Telescope. In each season, data are taken for one hour per night for roughly sixty nights during the six months that M31 is visible. The two 33'×33' fields of view straddle the central bulge, northwards and southwards. We have calculated the locations, periods and brightness of 35414 variable stars in M31 as a by-product of the microlensing search. The variables are classified according to their period and brightness. Rough correspondences with classical types of variable star (such as population I and II Cepheids, Miras and semi-regular long-period variables) are established. The spatial distribution of population I Cepheids is clearly associated with the spiral arms, while the central concentration of the Miras and long-period variables varies noticeably, the brighter and the shorter period Miras being much more centrally concentrated.

A crucial role in the microlensing experiment is played by the asymmetry signal – the excess of events expected in the southern or more distant fields as measured against those in the northern or nearer fields. It was initially assumed that the variable star populations in M31 would be symmetric with respect to the major axis, and thus variable stars would not be a serious contaminant for measuring the microlensing asymmetry signal. We demonstrate that this assumption is not correct. All the variable star distributions are asymmetric primarily because of the effects of differential extinction associated with the dust lanes. The size and direction of the asymmetry of the variable stars is measured as a function of period and brightness. The implications of this discovery for the successful completion of the microlensing experiments towards M31 are discussed.

Key words: stars: variables: Cepheids – stars: variables: others – galaxies: individual: M31 – dark matter – gravitational lensing

1 INTRODUCTION

Hodge (1992) reports in his book on the Andromeda Galaxy that “*the variable stars of M31 have been the subject of a number of rather limited studies. The very brightest are fairly well understood, but only a few areas have been searched deeply. There is still an immense amount of information about this component of the Andromeda Galaxy that remains untouched.*”

There is early work on Cepheids in M31 by Baade & Swope

[★] Based on observations made through the Isaac Newton Group’s Wide Field Camera Survey Programme with the Isaac Newton Telescope operated on the island of La Palma by the Isaac Newton Group in the Spanish Observatorio del Roque de los Muchachos of the Instituto de Astrofísica de Canarias.

[†] E-mail: jin@ast.cam.ac.uk

[‡] Pixel-lensing Observations on the Isaac Newton Telescope - Andromeda Galaxy Amplified Pixels Experiment

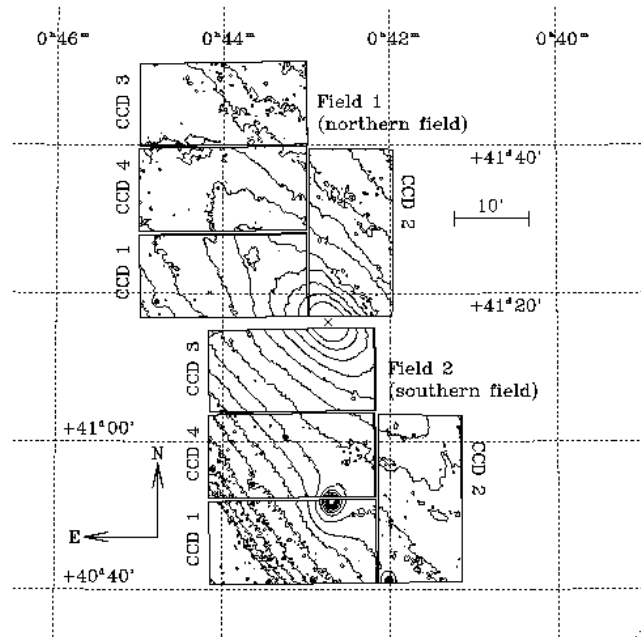


Figure 1. The INT WFC observation fields of M31. Also drawn is the r band surface brightness contour of M31 in the fields. The centre of M31 is at $\alpha = 0^{\text{h}}42^{\text{m}}44^{\text{s}}.31$, $\delta = +41^{\circ}16'09''.4$ (J2000.0) and is marked by a cross.

(1963, 1965). They found and studied ~ 400 Cepheids, primarily for the purpose of estimating the distance modulus for M31. A modern day successor to this pioneering work is the DIRECT project (Stanek et al. 1999; Mochejska et al. 2000; Bonanos et al. 2003). They have been searching M31 (and M33) for detached eclipsing binaries and Cepheids to refine the extragalactic distance ladder. They analysed five $11' \times 11'$ fields in M31 and found a total of 410 variables of which roughly half were Cepheids. There is also a substantial body of work on classical novae. Positions, magnitudes and light curves already exist for ~ 300 classical novae in M31 (Rosino 1973; Rosino et al. 1989; Ciardullo, Ford & Jacoby 1983). Despite all this, the underlying truth of the quotation from Hodge’s book is evident. The Andromeda galaxy is sufficiently close that the variable star populations can be studied in enormous detail – and with much greater ease than those in our own Galaxy, for which an all-sky survey would be needed.

Interest in the variable stars of M31 was re-kindled by influential papers by Crotts (1992) and Baillon et al. (1993) on the possible microlensing signal of the halo. The high inclination of the M31 disk ($i \approx 77^\circ$) means that lines of sight to sources in the far disk are longer and pass closer to the denser central parts of the halo than lines of sight to sources in the near disk. In other words, there is a strong gradient in the microlensing signal across the disk, if the events are caused by objects in a spheroidal halo. Early on, it was argued that the stellar populations of M31 are well-mixed and so no variable star population would show this behaviour (Crotts 1992). Thus, it seemed that the strategy in the experiment was straightforward; first, microlensing candidates should be identified on the basis of achromaticity and goodness of fit to a Paczyński curve, and second the gradient of detected candidates should be measured and confronted with theoretical models. The asymmetry in microlensing rate between the near and the far disk therefore seemed an unambiguous way of diagnosing events caused by lenses in the halo, as opposed to stellar lenses, and thus resolving the ambiguity in the results of the experiments monitoring the Large Magellanic

Table 1. The date, exposure, and seeing for the r band reference images for the northern and southern fields.

| Field | CCD | Image | Exposure | Seeing | Date |
|----------|---------|---------|----------|---------|------------|
| northern | 1 and 2 | r188970 | 700 s | $1''.6$ | 14/08/1999 |
| northern | 3 and 4 | r197399 | 360 s | $1''.4$ | 05/10/1999 |
| southern | 1 and 2 | r188986 | 700 s | $1''.4$ | 14/08/1999 |
| southern | 3 and 4 | r187566 | 600 s | $1''.5$ | 08/08/1999 |

Clouds. Accordingly, a number of groups began intensive monitoring of M31 with the aim of detecting microlensing events, including the POINT-AGAPE (Aurière et al. 2001; Paulin-Henriksson et al. 2002, 2003; Calchi Novati et al. 2003; An et al. 2004), WeCAPP (Riffeser et al. 2001, 2003) and MEGA (de Jong et al. 2004) collaborations.

The first hint that this was not the case came when Burgos & Wald-Doghramadjian (2002), working with data taken by the POINT-AGAPE collaboration, showed that the numbers of variable stars in symmetrically positioned fields in the near and far disk were not equal. The implication of this finding made the microlensing experiments much more difficult, as the asymmetry in the variable stars needs to be studied and measured as a function of brightness and period. Accordingly, the analysis of the variable star database in the microlensing experiments towards M31 is interesting from the standpoint of the light it throws on stellar populations in M31 and is crucial for a successful conclusion to the microlensing experiments.

The purpose of this paper is to present the variable star catalogue of the POINT-AGAPE survey. This gives the position, period and brightness of 35414 variable stars with high signal-to-noise lightcurves uncovered during the three-year duration of our survey. The variable star catalogue forms a subset of the grand total of 97280 lightcurves that show variations. The paper is arranged as follows: § 2 describes the acquisition of the data, § 3 discusses the images of M31 and the detection of resolved stars, § 4 outlines the construction of the lightcurves and the selection of the variable stars for the catalogue, § 5 studies the properties of the variable stars, whilst § 6 analyses the asymmetry signal and discusses the consequences for the microlensing surveys.

2 DATA ACQUISITION

Observations of M31 were obtained using the Wide Field Camera (WFC) mounted on the 2.5 m Isaac Newton Telescope (INT) located at La Palma, the Canary Islands, Spain, over three observing seasons, from 1999 August to 2002 January. Three broad-band filters, g , r and i , were employed. The combination of the filters and the response of the thinned EEV $4k \times 2k$ CCDs of the WFC produce overall pass-bands similar, but not identical, to the Sloan Digital Sky Survey g' , r' and i' bands. The r band images were taken throughout the 3-year campaign. Initially, a mix of both g and i band images were also obtained, but the g band monitoring was discontinued at the end of the first season. Weather and technical conditions allowing, observations in the second and third seasons consisted of both r and i band exposures in each of the two M31 fields.

The data analysed here consist of the r and i band exposures obtained over all three seasons. The location of the two fields, to the north and south of the nucleus of M31 can be seen in Figure 1 (see also Fig. 5 of Paulin-Henriksson et al. 2003). Typically, pairs of

fig02.jpg

Figure 2. The INT WFC gri image (left) and $g - r$ (centre) and $r - i$ (right) colour map of M31. One can observe very prominent dust structure in the northwestern part of M31. The (infrared) sensitivity or the background of CCD 2 may be slightly higher than other chips.

exposures were obtained in each band in each field in the sequence r field 1, i field 1, r field 2 and i field 2. Exposure times, normally 320 s in both r and i bands, were chosen to maximise the signal-to-noise ratio of each exposure, while ensuring that two exposures in each band could be obtained within the 3600 s allocated to the monitoring of M31 on each night. Advantages of acquiring two exposures per band per field included the ability to identify cosmic rays and to avoid saturation in exposures obtained in the i band during full moon.

A standard observing script was invoked to perform the observations and the data are generally of high quality. The on-chip seeing achieved falls predominantly in the range $1''.3$ - $2''.0$, which is well-sampled by the $0''.33$ pixels of the WFC. Observations on a small number of nights were affected by technical problems that resulted in frames with highly elongated images. Such frames were excluded from the analysis described here.

Monitoring of M31 was possible only when the WFC was mounted on the INT and when the telescope was scheduled for use by either the United Kingdom or Netherlands time allocation committees. We were fortunate to also obtain occasional monitoring observations from a few Spanish-scheduled observers. The monitoring schedule was further enhanced through observations obtained by INT staff and others during nights scheduled for engineering activities and service-observing.

The cooperation of astronomers and staff at the INT resulted in a total of 71 g , 316 r , and 254 i band for the northern field and 67 g , 293 r , and 232 i band for the southern field monitoring observations that produced frames suitable for analysis. However, the vagaries of the weather, combined with the rigid schedule for mounting of the WFC, means that the monitoring time-series consists predominantly of relatively well-sampled periods, typically of duration 7-14 days, interspersed with periods, typically of duration 7-21 days,

in which there are very few data. A summary of the observations taken is publicly available over the World Wide Web.¹

All frames were processed using the pipeline processing software (Irwin & Lewis 2001) developed for the reduction of the data obtained as part of the Wide Field Survey (WFS) undertaken with the WFC. The pipeline includes procedures to de-bias, trim and flatfield the frames. Additionally, protocols to perform non-linearity corrections, flag bad pixels, and apply gain corrections are applied. Master calibration frames (bias and flatfields, for r and i exposures, and fringe frames, for i exposures) necessary to reduce the observations, were constructed from all the suitable calibration frames obtained during the relevant 14-21 day period that the WFC was mounted on the INT. On a few occasions, insufficient calibration frames were obtained to construct an adequate master flatfield or fringe frame. In these cases the best master calibration frames from an adjacent period, when the WFC was mounted, were used.

The WFS pipeline proved entirely satisfactory with the exception of the defringing correction necessary for the i band frames. The WFS defringing scheme was developed to cope with exposures whose background is dominated by sky. In the case of our M31 exposures the “background” includes a significant contribution from M31 itself. Furthermore, the relative contribution of M31 to the background varies from CCD to CCD and between the exposures of the northern and southern fields. The variable sky brightness over a lunation also complicates the situation, as the contrast between M31 and the underlying sky-background changes.

Investigation of the amplitude of the defringing correction made by the WFS pipeline to remove the fringing from frames taken away from M31 showed a well-defined correlation with the

¹ <http://cdfinfo.in2p3.fr/Experiences/Agape/point-agape-log.html>

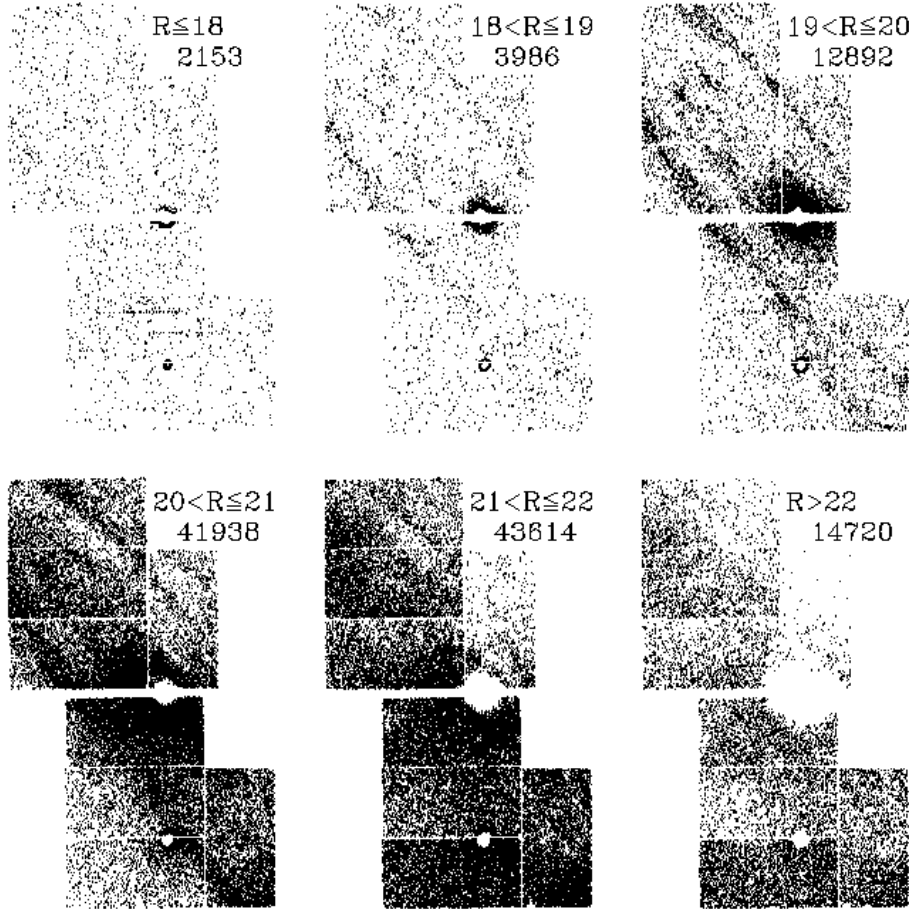


Figure 3. Spatial positions of resolved stars with different magnitudes. The stars with $R \leq 18$ form an almost uniform screen and so are predominantly foreground contaminants. There is also no evidence of chip to chip variation for stars with $R \leq 21$, suggesting that the catalogue is complete to this limit.

background surface brightness. Small, $< 10\%$, systematic offsets in the amplitude of the scaling applied to the master fringe frames from CCD to CCD were also evident. Comparison of the underlying sky-brightness in frames (away from M31) taken immediately prior or subsequent to the M31 monitoring showed that an accurate estimate of the underlying sky-brightness in the M31 frames could be obtained using the far south-eastern corner of CCD 1 in the southern field. Thus, the amplitude of the defringing correction applied to both the northern and southern M31 frames was derived using the estimate of the sky-brightness from the south-eastern corner of CCD 1 in the southern field, allowing for the well-determined small systematic offsets from CCD to CCD.

3 THE SURFACE BRIGHTNESS AND THE RESOLVED STARS OF M31

Figure 2 shows a *gri* (which is close to the standard *VRI*) image of M31, together with the $g-r$ and $r-i$ (close to $V-R$ and $R-I$ respectively) colour maps. These are constructed by median filtering the images with a 49 pixel ($16''.3$) square box and re-sampling with a $10''$ grid. The filtering is done to remove graininess in the images, while the re-sampling is done to enable a fair comparison with maps of the variable star distribution which will be presented later. The colour maps clearly delineate the dust lanes. It is evident that the dust distribution is asymmetric with the north-western parts of M31 being dustier. This is already worrisome, as it may muddle any intrinsic microlensing asymmetry.

We also construct a catalogue of 119303 resolved stars – namely, all stars detected by the task *daofind* in IRAF at 5σ above the background noise in the r band reference image list in Table 1. For the detected stars, the r magnitudes are converted into standard Cousins R magnitudes. Figure 3 shows the break-down of

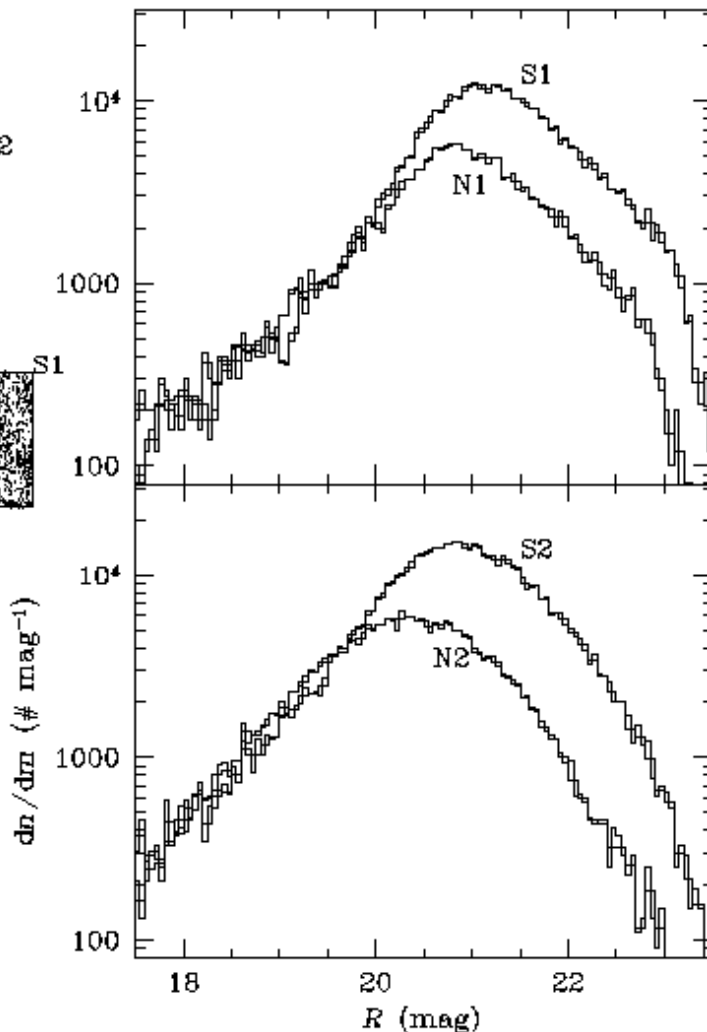


Figure 4. The observed uncorrected luminosity function in pairs of fields (namely N1, S1 and N2, S2) symmetrically positioned with respect to the centre of M31. All four fields are $15' \times 22'$ in size.

the 119303 resolved stars into magnitude bins. Stars with $R \leq 18$ are predominantly foreground objects, as evidenced by their homogeneity. For $18 \leq R \leq 20$, we can see a mixture of M31 stars – which are predominantly young, massive supergiants – together with some contamination from the foreground and from unresolved globular cluster cores and blended stars. The supergiant population is concentrated in star-forming regions associated with the spiral arms, which are clearly seen in Figure 3 and coincide with the blue region in Figure 2.

For $R \geq 20$, the asymptotic giant branch (AGB) stars start to make their appearance, while the red giant branch (RGB) stars are somewhat fainter and do not appear at least up to $R \approx 21$. With the absolute magnitude of the tip of the RGB being $M_I \approx -4.0$ (Bellazzini, Ferraro & Pancino 2001), and the distance modulus of M31 being $(m - M)_{M31} \approx 24.5$ (Holland 1998; Stanek & Garnavich 1998), the brightest RGB stars are around $R \approx 21.5$, assuming the colour $R - I \geq 1.0$. The brightest AGB stars are around a magnitude or so brighter. Again, on comparing Figure 3 with Figure 2, we see that there is a clear depression in the distribution of AGB stars (with

$20 < R \leq 21$) coincident with the prominent dust lane in the north-west of the galaxy.

The limiting magnitude of field 1, CCD 2 seems to be somewhat shallower than the other CCDs. We can also see some evidence of variation of the limiting magnitude with surface brightness near the central bulge and near M32. This therefore raises the worry that variations in the limiting magnitude from CCD to CCD, caused by the choice of reference images with different background and exposure, may be producing artificial gradients. To investigate this, we plot in Figure 4 the distribution of resolved stars in different magnitude bins, or the observed luminosity function. Here, the two pairs of fields (N1, S1 and N2, S2) are chosen to be symmetric with respect to the centre of M31, as illustrated in the side-panel of the figure. For each field, two nearly-superposed histograms are shown, one for a bin-size of 0.1 mag, one for a bin-size of 0.05 mag. The excellent correspondence between the histograms shows that the bin-size is not influencing the results.

The luminosity functions in all four fields turn over at $R \sim 20.5$, and are in good agreement for $R < 20$. The turn-over in the lu-

fig05.jpg

Figure 5. Grey-scale surface density maps of the resolved stars; $R \leq 20$ (left), $20 < R \leq 21$ (centre), $R > 21$.

minosity function is almost certainly due to incompleteness. However, we are interested primarily in comparisons between the northern and southern fields, and so provided we believe that roughly the same fraction of stars is missing, we can go deeper than the turnover.

For $R \gtrsim 20$, the luminosity function in the southern fields (S1 and S2) is higher than in their northern counterparts (N1 and N2). For higher surface brightness, the detection limit should be shallower. However, the reverse is true here, as the southern fields are brighter – not fainter – than the northern ones. This is circumstantial evidence that the relatively low normalisation of the northern field luminosity function is a real effect, rather than an artefact of differing efficiency. Note that this rules out the lower sensitivity of CCD 2 as a cause of any asymmetry, as we would then expect more stars in N1 than S1, which is not seen. However, it is still possible that CCD 2 in field 1 alone is the cause of the problem because of the underlying surface brightness structure in that field. Part of the low normalisation is probably caused by the prominent dust lane and enhanced extinction in the northern field. Additionally, the slope of the falling parts of each pair of histograms at least for $R \lesssim 22$ in Figure 4 is the same. If the underlying true luminosity function has the same slope, then this can be explained very naturally by assuming that the same fraction of stars is missing at each magnitude, irrespective of whether the field is north or south.

For the purposes of our analysis, it is helpful to convert the spatial distribution shown in Figure 3 into smooth maps of the surface number density. This is achieved by counting the number of resolved stars within a suitable window function. In Figure 5, this is done for three different magnitude bins. In the left panel corresponding to resolved stars with $R \leq 20$, the window function is a square box of size $3'$. For the other two panels, the square box has size $2'$. The re-sampling is done in the same way as described for Figure 2. Again, for $R < 20$, we see the prominent ring (possibly a

spiral arm) associated with the supergiant population. Some of the dust structures visible in the colour maps of Figure 2 can be traced in the surface density maps of the fainter stars. There are also artefacts – such as the deficiency in resolved stars with $R > 20.5$ in field 1, CCD 2 – that are manifest in the Figure.

To conclude, there is clear asymmetry in the resolved star distribution, and some of this is certainly due to bias during the data reduction. However, the similar patterns caused by dust lanes clearly visible in the surface brightness map, the colour maps and the resolved star maps argue that there is a real asymmetry caused by variable extinction. This hypothesis could be confirmed by examination of the colour-magnitude diagrams in the northern and southern fields, which should show differing positions for the RGB stars.

4 CONSTRUCTION OF THE VARIABLE OBJECT CATALOGUE

The M31 fields are composed of largely unresolved stars, and so the effects of seeing are significant. In order to build lightcurves, we need to develop an algorithm for which the same fraction of flux falls within the window function, irrespective of seeing. The superpixel method provides a linear transformation between the flux measurements with different seeing (Melchior et al. 1999; Ansari et al. 1999; Le Du 2000). The basic idea is to calibrate the frames so that they have the same large-scale average surface brightness and then to adjust any spatial flux variations to the same seeing.

The observed flux ϕ within the window function at a given position is a convolution of the intrinsic surface brightness Φ with the point-spread function (PSF) P and the window function W . Assuming that the PSF is flux-conserving, the large scale average flux $\bar{\phi} = \bar{\Phi} \otimes W$ is independent of the PSF. Here, $\bar{\Phi}$ is the large scale average of the intrinsic surface brightness. Furthermore, the spatial

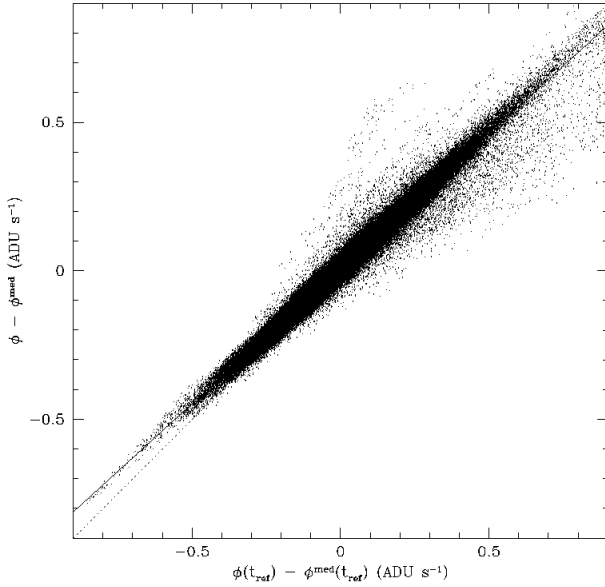


Figure 6. The linear correlation between flux differences on the reference image and on an image with good seeing respectively. Each dot in the “cigar” corresponds to a superpixel. The solid line is the best fit linear regression line, whilst the dotted line illustrates the identity relation.

fluctuation of the flux is also related to the intrinsic spatial surface brightness fluctuation via the same convolution, viz.

$$\phi - \bar{\phi} = (\Phi - \bar{\Phi}) \otimes P \otimes W. \quad (1)$$

Taking Fourier transforms, the convolutions become products, and so we have

$$\mathcal{F}\{\delta\phi\} = \mathcal{F}\{\delta\Phi\}\mathcal{F}\{P\}\mathcal{F}\{W\}, \quad (2)$$

where \mathcal{F} denotes the Fourier transform. The effects of the shape of the PSF near the centre are unimportant, if the characteristic scale of the window function is chosen to be large enough. On the other hand, for any reasonable PSF, the wings behave in a similar manner to lowest order. Then, taking the ratio of equations (2) for two epochs implies that the Fourier transforms of the flux variations are linearly related. Consequently, the flux differences at different epochs are also linearly related. The superpixel method provides an empirical way of calculating the coefficients of this linear transformation. Note that this linearity is only true in lowest order, and so the method fails for large seeing variations or near very bright stars.

The original pixel size ($0''.33$) over-samples the seeing disk ($\text{FWHM} \gtrsim 1''$), and thus the relative amplitude of the flux variations due to seeing variation is quite large even for moderate variation of seeing. This leads us to associate a superpixel flux ϕ with each pixel. This is derived by summing fluxes from several adjacent pixels that fall within a pre-defined “superpixel” window (in other words, W is a top-hat function defined over a square box). The size of this superpixel is chosen to ensure that it under-samples the seeing disk.

Next, the data are smoothed by a median filter with a window size that is sufficiently large so as not to be affected by small-scale fluctuations. This gives the median superpixel flux ϕ^{med} at

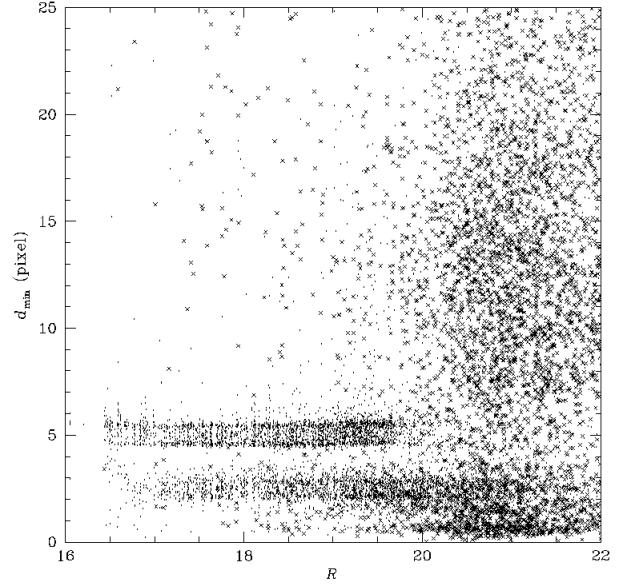


Figure 7. Each point represents a variable lightcurve in CCD 4 of the northern field. The R magnitude of the nearest resolved star is plotted against the distance to that resolved star. In other words, a point at coordinates (18, 2) means that there is a variable star lightcurve that lies 2 pixels away from a resolved star with $R = 18$.

each point. This median flux is subtracted from the superpixel flux.² The quantity $\phi - \phi^{\text{med}}$ represents a variation in flux with respect to the same underlying median surface brightness. It changes with the seeing. Empirically, we find that the flux differences at different epochs are linearly related to each other, as shown in Figure 6. By recalibrating the flux differences, we obtain superpixel lightcurves which represent the intrinsic variation at fixed seeing. In practical implementation, we find the slope α and the intercept β of the regression line on the cigar shape depicted in Figure 6, namely

$$\phi(t_i) - \phi^{\text{med}}(t_i) = \alpha(t_i) [\phi(t_{\text{ref}}) - \phi^{\text{med}}(t_{\text{ref}})] + \beta(t_i), \quad (3)$$

and the subsequent recalibration follows as

$$\phi'(t_i) = \frac{[\phi(t_i) - \phi^{\text{med}}(t_i)] - \beta(t_i)}{\alpha(t_i)} + \phi^{\text{med}}(t_{\text{ref}}). \quad (4)$$

If the background subtraction is sufficiently accurate and if the fluxes represent the intrinsic, physical surface brightnesses, then the median flux must be constant, $\phi^{\text{med}}(t_i) = \phi^{\text{med}}(t_{\text{ref}})$. In this case, the linear relation will become a proportionality ($\beta = 0$), while the coefficient α will be solely a function of the seeing difference (in particular, if the images at t_i and t_{ref} are taken in the same seeing, then α will be unity).³ For best results, the reference image is chosen to be one taken in the median seeing. We note that the linear relation shown in Figure 6 is not a perfect one-to-one correspondence, but is rather an (albeit tight) statistical correlation with a scatter. In other words, this procedure of stabilising the seeing variation introduces an additional uncertainty. Therefore, the error bar on the i -th flux measurement, corrected for seeing, is

² In our application, the median flux ϕ^{med} is used instead of the mean $\bar{\phi}$ in eq. (1).

³ Even if the photometric calibration is imperfect, then the seeing correction (4) will still give the correct results but with non-vanishing β .

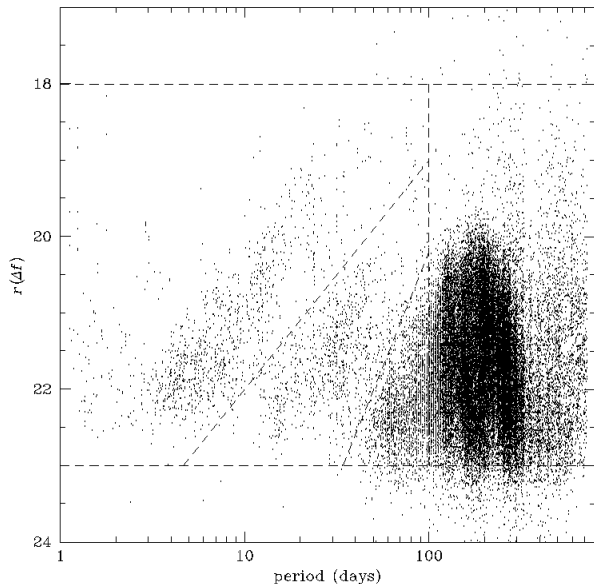


Figure 8. The locations of the $\sim 40,000$ variable stars in the period- $r(\Delta f)$ plane. The period computed via Lomb’s periodogram is discrete and so the positions are shifted by small random values to enhance visibility. Notice the two straight-line features in the left of the plot, which are suggestive of period-luminosity relationships. Also shown with dashed lines are the boundaries for the group classification given in the text.

$$\sigma_i^2 = \frac{1}{\alpha^2} \sigma_{\gamma_i}^2 + \sigma_{\text{see}}^2, \quad (5)$$

where σ_{γ} is the photon noise in the original image and σ_{see} is the additional uncertainty caused by the recalibration. This is empirically estimated from the width of the cigar shape in Figure 6 using the method of maximum likelihood.

In the implementation of the method here, the median flux is computed over a 41×41 pixel field. The method is not too sensitive to the size of the field, provided it is big enough that even bright resolved stars disappear from the median image. There is an optimum size to the superpixel. If the superpixel is too small, the algorithm fails because the seeing disk is over-sampled. However, as the superpixel gets larger, the photon noise increases and the sensitivity drops. We choose the superpixels to be 7×7 pixels in size. This is because typical poor seeing at the INT site is $\sim 2''$ so that a star with a Gaussian PSF is contained up to a 1σ distance in the 7×7 superpixel centred on it. The reference images used for the r band data are the same as the image on which the detection of resolved stars has been performed (Table 1).

The WFC has $2k \times 4k$ pixels in each chip. There are 4 chips and 2 fields, giving $\sim 6.4 \times 10^7$ superpixel lightcurves for each passband. The selection procedure is carried out on the r band data alone. For each lightcurve, the first step is to determine the baseline flux μ . This is calculated iteratively by computing the median, deleting all points 3σ above (but not below) the baseline and repeating until convergence. This is tailored for microlensing events, which are positive excursions above the baseline, but fails for eclipsing binaries or transits. Any lightcurve that has at least 3 consecutive points at least 3σ above the baseline is selected as a fluctuation. For each variable object, there is a cluster of associated superpixel lightcurves. The likelihood L of variation for every superpixel position is calculated by

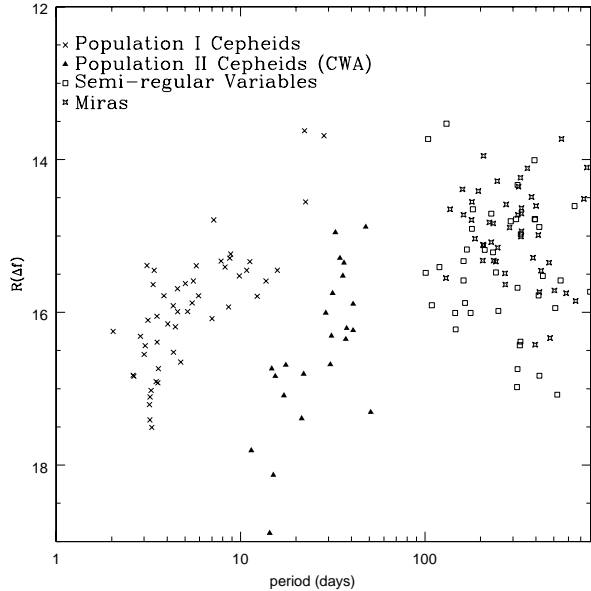


Figure 9. The locations of some common types of variable stars in the Large Magellanic Cloud plotted in the period- $R(\Delta f)$ plane. The data are drawn from the General Catalogue of Variable Stars.

$$\ln L = \sum_{i \in \text{fluct}} \ln P(\phi_i), \quad (6)$$

with

$$P(\phi_i) = \frac{1}{(2\pi)^{1/2} \sigma_i} \int_{\phi_i}^{\infty} d\phi \exp \left[-\frac{1}{2} \left(\frac{\phi - \mu}{\sigma_i} \right)^2 \right]. \quad (7)$$

For each superpixel, a likelihood map is constructed over the field and the optimum position of each variable source is extracted from it using SExtractor (Bertin & Arnouts 1996).

We select a total of 97280 lightcurves by the procedure outlined above. However, many lightcurves in this list are spurious; most of the artefacts are caused by a bright resolved star lying near the edge of a given superpixel, which induces a non-linear response of the adjacent superpixel flux level depending on the variation of seeing. Since the seeing varies without any significant coherence on a nearly daily basis, the resulting lightcurves appear almost like white noise although the amplitude can be many times larger than the typical photometric uncertainty of the superpixel flux. Such artefacts can be recognised easily by eye. It is however clearly preferable to devise an objective criterion. Referring to Figure 7, we see that there is an excess of variables around 2.5 and 5 pixel distance from resolved stars, which corresponds to the concentration of artefacts. These can be removed by construction of a suitable mask consisting of annuli around resolved stars and known CCD defects. This is done for the selection of microlensing candidates in a later publication. In this paper, however, we use a different (but related) criterion, which is explained in the next section.

5 THE PROPERTIES OF THE VARIABLE STARS

We characterise each variable lightcurve by two numbers, its period P and the “pseudo-magnitude” $r(\Delta f)$. The period is computed using Lomb’s periodogram (e.g., Press et al. 1992), which is appropriate for unevenly sampled datastreams. The algorithm works by calculating the power spectrum over a discrete frequency interval. The frequency at maximum power is converted into the period for the lightcurve. Therefore, the absolute uncertainty in the period scales quadratically with the period itself and so the computed value may not be precise when $P \gtrsim 150$ days. In principle, there are other methods of computing a more precise period, but Lomb’s periodogram suffices for the purpose of classification.

As a measure of the brightness of each variable, we define the “pseudo-magnitude”. Because the fraction of light contributed by the variable object to the total superpixel flux at a given epoch is not known, it is not possible to find the real magnitude of the variable. Under these circumstances, we first measure the quantity Δf , which is the flux variation between minimum and maximum in ADU s^{-1} . Then, we convert Δf into magnitudes by $r(\Delta f) = r_0 - 2.5 \log_{10}(\Delta f)$, which we subsequently employ as a proxy for the underlying brightness of the variable. Here, r_0 is the zeropoint, that is, the r band magnitude of a star whose flux is 1 ADU s^{-1} in the reference image. Henceforth, we refer to this quantity $r(\Delta f)$ – or $i(\Delta f)$, $g(\Delta f)$ and so on where appropriate – as a pseudo-magnitude. We note that it is not the same as the variable amplitude in magnitudes (that is $\Delta r \equiv r_{\min} - r_{\max} = 2.5 \log_{10}[1 + (\Delta f/f_{\min})]$ where r_{\min} and f_{\min} are the magnitude and the flux at minimum, and r_{\max} is the magnitude at maximum). Rather, the pseudo-magnitude is related to the magnitude of variable and the variable amplitude via

$$\begin{aligned} r(\Delta f) &= r_{\max} - 2.5 \log_{10}[1 - 10^{-0.4\Delta r}] \\ &= r_{\min} - 2.5 \log_{10}[10^{0.4\Delta r} - 1]. \end{aligned} \quad (8)$$

Therefore, as Δr becomes larger, $r(\Delta f)$ approaches the true magnitude at maximum r_{\max} of the variable. [If $\Delta r = 0.5$, then $r(\Delta f) \approx r_{\max} + 1.1$. On the other hand, if $\Delta r = 1.0$, then $r(\Delta f) \approx r_{\max} + 0.55$.] Note that our use of superpixels in the variable lightcurve detection mechanism implies that our detection is nominally more sensitive to relatively faint but large amplitude variables than bright but small amplitude variables. Hence, we argue the pseudo-magnitude is a reasonably good approximation for the real magnitude at maximum for our sample. In addition, the majority of the variables in our sample is believed to be AGB/RGB variables such as Miras and semi-regular variables (see below), and their amplitudes are known to be quite large (e.g., $\gtrsim 2.5$ mag for Miras, Whitelock 1996). This also supports the view that the pseudo-magnitude is in fact a reasonable alternative for the magnitude of variable for most of our lightcurves.

Each superpixel contains many variables and so it might be thought that the period and pseudo-magnitude derived from the lightcurves may be misleading. We expect this not to be the case because it is very rare for two comparably bright variables to contribute to the same superpixel. This can be seen on computing the mean distance between our detected variables, which is ~ 50 pixels or ~ 7 superpixels.

The analysis of the spatial distribution of variables is based on the catalogue of objects selected by Lomb’s periodogram as having a significant coherent behaviour. Datapoints lying more than 4 standard deviations from the arithmetic mean are discarded to minimise the effects of outliers in the periodogram. Given any sampling, there is a correspondence between the peaks of the power spectrum and the significance level. Specifically, we insist that the

fig15.gif

Figure 15. The analogue of a colour-magnitude diagram for the r -band selected variables. Green dots are for group 1, blue for group 2, cyan for group 3, and red for group 4 with $P \leq 0.5$ yr, and yellow for group 4 with $0.5 \text{ yr} < P \leq 1$ yr.

strongest periodic signal has a false alarm probability of less than 10^{-7} . This effectively removes all the spurious lightcurves – as can be seen in Figure 7, in which the variables that pass this criterion are shown as crosses. Additionally, we require that the period be less than 800 days, roughly corresponding to the baseline of the experiment. Only lightcurves with $18 < r(\Delta f) \leq 23$ are included. The rationale for these limits is that $r(\Delta f) = 23$ roughly corresponds to our detection limit, while variations with $r(\Delta f) < 18$ are most likely foreground contaminants. This gives a variable star catalogue with 38779 members, which still has a number of duplicate entries. These are removed using the following algorithm. First, all the pairs of variable objects within 6 pixels are located, and their lightcurves correlated. If the correlation coefficient is larger than 0.75, then the lightcurve with lower significance is removed from the catalogue. This leaves 35414 variable objects. The positions, periods and pseudo-magnitudes of these variables are available as an accompanying electronic table.

Figure 8 shows the locations of the variables in the period- $r(\Delta f)$ plane. We can quite easily divide the objects in this space into several distinct groups, loosely corresponding to some familiar variable star classes. For comparison, Figure 9 shows the locations of some common classes of variable stars in the similar period- $R(\Delta f)$ plane, drawn from the General Catalogue of Variable Stars⁴. Here, $R(\Delta f)$ is the R band flux difference between the maximum and the minimum converted into magnitudes by the similar manner. Here, the variable stars primarily reside in the Large Magellanic Cloud, and so there is a vertical offset corresponding to the differences in distance modulus and extinction. Clearly picked out in both Figures 8 and 9 are sequences corresponding to the period-luminosity relations of population I and II Cepheids. Both semi-regular and Mira variables are clustered together at longer periods than the Cepheids.

⁴ <http://www.sai.msu.su/groups/cluster/gcvs/gcvs>

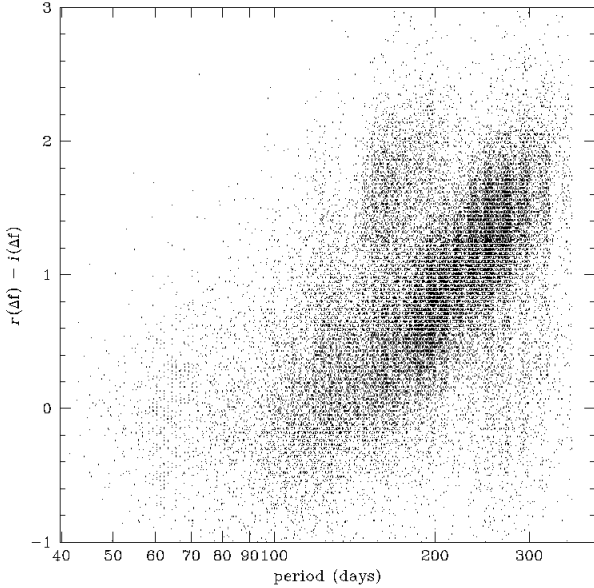


Figure 16. Period versus colour $r(\Delta f) - i(\Delta f)$ for variables in groups 3 and 4 with $P \leq 1$ yr.

This motivates us to group the variables in Figure 8 into the following four divisions:

- (1) $r(\Delta f) + 3 \log_{10} P \leq 25$ and $\log_{10} P \leq 2$,
- (2) $r(\Delta f) + 3 \log_{10} P > 25$ and $r(\Delta f) + 6 \log_{10} P \leq 32.2$ and $\log_{10} P \leq 2$,
- (3) $r(\Delta f) + 6 \log_{10} P > 32.2$ and $\log_{10} P \leq 2$,
- (4) $2 < \log_{10} P \leq 2.9$.

The period is measured in days. Comparison between Figures 8 and 9 suggests the following rough identifications. The variables in group 1 are mainly population I Cepheids pulsating in either the fundamental or the first overtone modes. In fact, the tracks on which the variables in group 1 reside are suggestive of the classical Cepheid period-luminosity relationships. This group also includes a distribution of variables with periods shorter than 3 days. These are either eclipsing binaries or population II Cepheids pulsating in the first overtone mode, sometimes called BL Her or CWB stars (Feast 1996). The variables in group 2 also cluster on a period-luminosity relationship and are mainly population II Cepheids in the fundamental mode (W Vir or CWA stars). Group 3 is composed mainly of semi-regular and Mira variables with rather short periods or incomplete sampling, while those in group 4 are a mixture of semi-regular and long period Mira variables. Typical lightcurves of objects in all four groups are given in Figures 10-13.

In addition to the 35414 variables in the catalogue with reasonably well-determined pseudo-magnitude and period, there are further variables for which the reported period is longer than 800 days. We classify these as group 5. The determined period and pseudo-magnitude are not reliable since a whole cycle is not covered by the experiment. A number of these are associated with CCD defects and can be rejected with a suitable mask. This leaves 2243 variables with ill-determined or incomplete periods after removing duplicate entries. Some examples of lightcurves in this group can be found in Figure 14 while the data are available as an accompanying electronic table. Variables in this group are not included in subsequent calculations of statistical quantities.

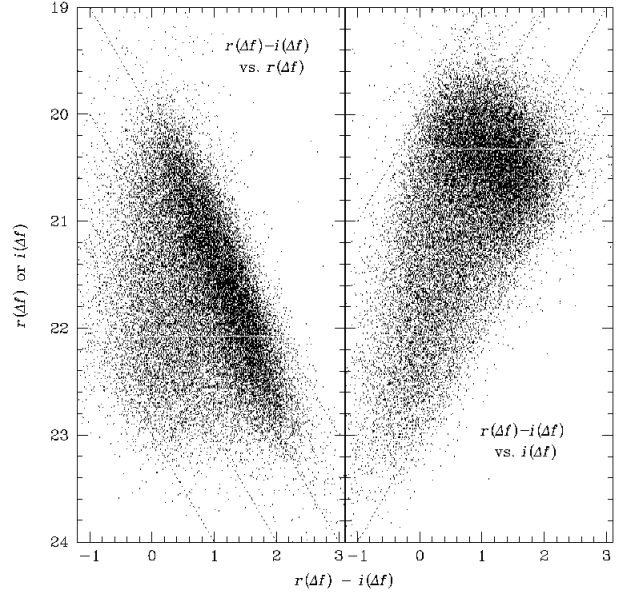


Figure 17. Analogues of the colour-magnitude diagram for groups 3 and 4 with $P \leq 1$ yr.

5.1 Colours

For r -band selected variables, we examine the g and i band lightcurves and, if they contain noticeable variations, we derive pseudo-magnitudes $g(\Delta f)$ and $i(\Delta f)$. These can be used to build an analogue of the colour-magnitude diagram, as shown in Figure 15. Note that the i band data are largely restricted to the last two seasons, so variables with period longer than 1 yr are not plotted.

The first thing to notice is that different groups of variable stars are clearly separated. The variables in groups 1 and 2 are bluer than those in groups 3 and 4. This is expected because Cepheids are F or G (super)giants, whilst Miras are M (super)giants. As the variables in group 1 are primarily population I Cepheids, their positions mark the location of the instability strip. The positions of groups 3 and 4 indicate the location of the RGB and AGB of varying ages and metallicity in this analogue of a colour-magnitude diagram. They are segregated according to their periods, with the longer period variables being brighter in i and so redder in colours involving i . However, this is not the case for the $g(\Delta f) - r(\Delta f)$ (not shown), as, along the sequence of M stars, the $r - i$ becomes redder, whilst the $g - r$ stays the same (e.g., Margon et al. 2002; Szkody et al. 2003). Figure 16 shows the period plotted against $r(\Delta f) - i(\Delta f)$ for groups 3 and 4 with $P \leq 1$ yr. This shows a moderately strong correlation, which is analogous to the similar period- $(H_p - K)$ colour correlation for Mira and semiregular variables (Whitelock, Marang, & Feast 2000). Here, H_p is the Hipparcos broad-band magnitude. This relation is also presumably related to the well-known period- K band luminosity relation for Mira variables (e.g., Feast et al. 1989; Noda et al. 2002; Glass & Evans 2003; Kiss & Bedding 2003), as the redder evolved AGB stars are typically brighter in near infrared bands. The secondary clump centred on $\log_{10} P \approx 2.2$ and $r(\Delta f) - i(\Delta f) \approx 1.8$ may be an artefact caused by half-year sampling gaps combined with incompleteness of our period determination, as it is displaced from the main correlation by almost $\log_{10} 2$. However, Whitelock et al. (2000) found a similar ‘‘secondary clump’’ in their AGB period- $(H_p - K)$ colour relation and suggested that Miras

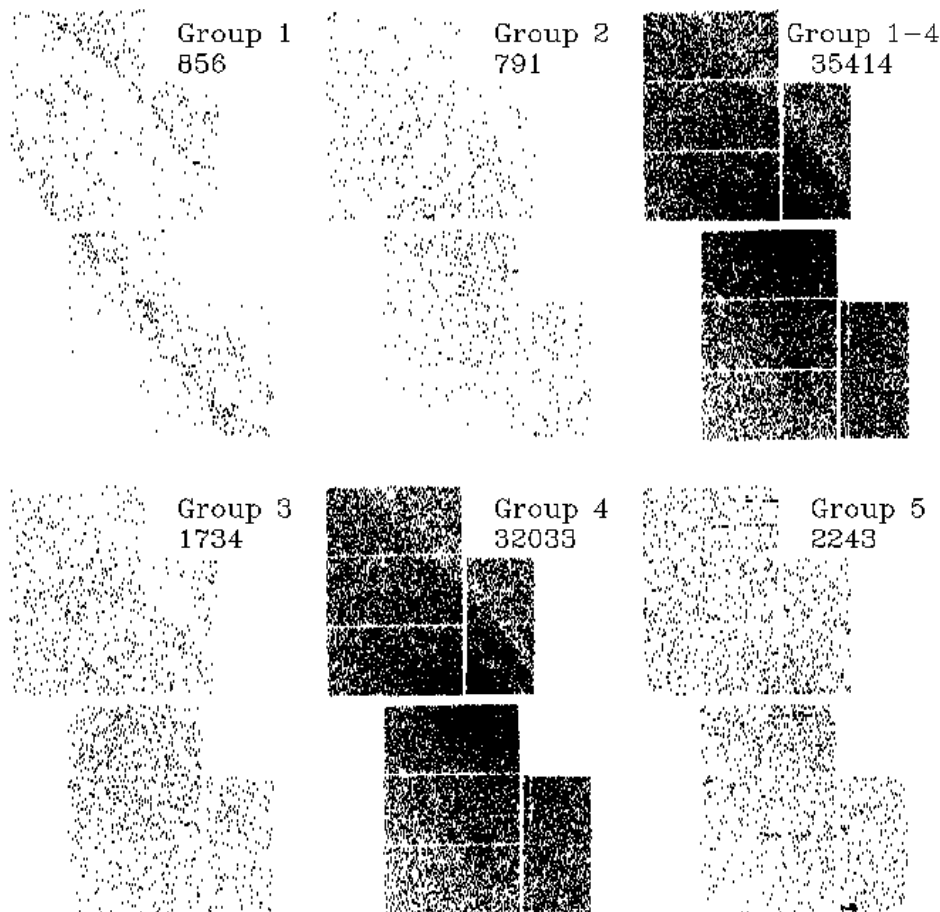


Figure 18. The spatial positions of the variable stars, split into the groups suggested by Fig. 8. The numbers of objects in each group are shown in the top-right hand corner of each sub-panel.

with $P < 225$ days are divided into two groups depending on their $H_p - K$ colour or spectral types. As the transformations from our observables to these colours are unknown, the answer to whether the secondary clump in Figure 16 is real and indeed an analogue to that found by Whitelock et al. (2000) is inconclusive at the moment. Nevertheless, we note that $\sim \log_{10} 2$ separation may also be explained physically by invoking pulsations on the overtone mode.

Figure 17 shows analogues of the same $r(\Delta f) - i(\Delta f)$ colour versus $i(\Delta f)$ magnitude diagram for only groups 3 and 4 with $P \leq 1$ yr, along with the $r(\Delta f) - i(\Delta f)$ colour versus $r(\Delta f)$ magnitude diagram. We note that there is a strong cut-off in the bright end, namely $i(\Delta f) \approx 20$ and this presumably corresponds to the tips of the AGB and RGB with different ages and metallicities. The locuses are most likely to be caused by the differences in metallicity and ages of the AGB and RGB populations, with the redder side younger and more metal-rich. We note that, along the locus, as the stars get redder, they become fainter in r , but maintain more or less the same i (pseudo-)magnitude.

5.2 Spatial Distribution

Next, we investigate the spatial distribution of the groups of variable stars on the WFC fields. Figure 18 shows the distributions of groups 1 to 5 of variable stars, together with the set of all the 35414 variable stars with well-determined periods (groups 1-4 combined). Figure 19 shows the distributions of variables in group 4, further sub-divided by their period and pseudo-magnitude.

Most obviously, variables in group 1 follow the same pattern as the bright supergiant population already seen in the top right-most panel of Figure 3. Both populations seem to be associated with the spiral or ring-like structure. This reinforces our identification of group 1 as population I Cepheids, because the latter are known to occur preferentially in spiral arms (Magnier et al. 1997; Mel’Nik, Dambis & Rastorguev 1999). Any spirality is much less evident in groups 2, 3 and 4, as would be expected for population II Cepheids, semi-regular variables and Miras, which are found in both the halo and the old disc populations of M31 (Hodge 1992).

The variables in group 4 follow the same pattern as the AGB

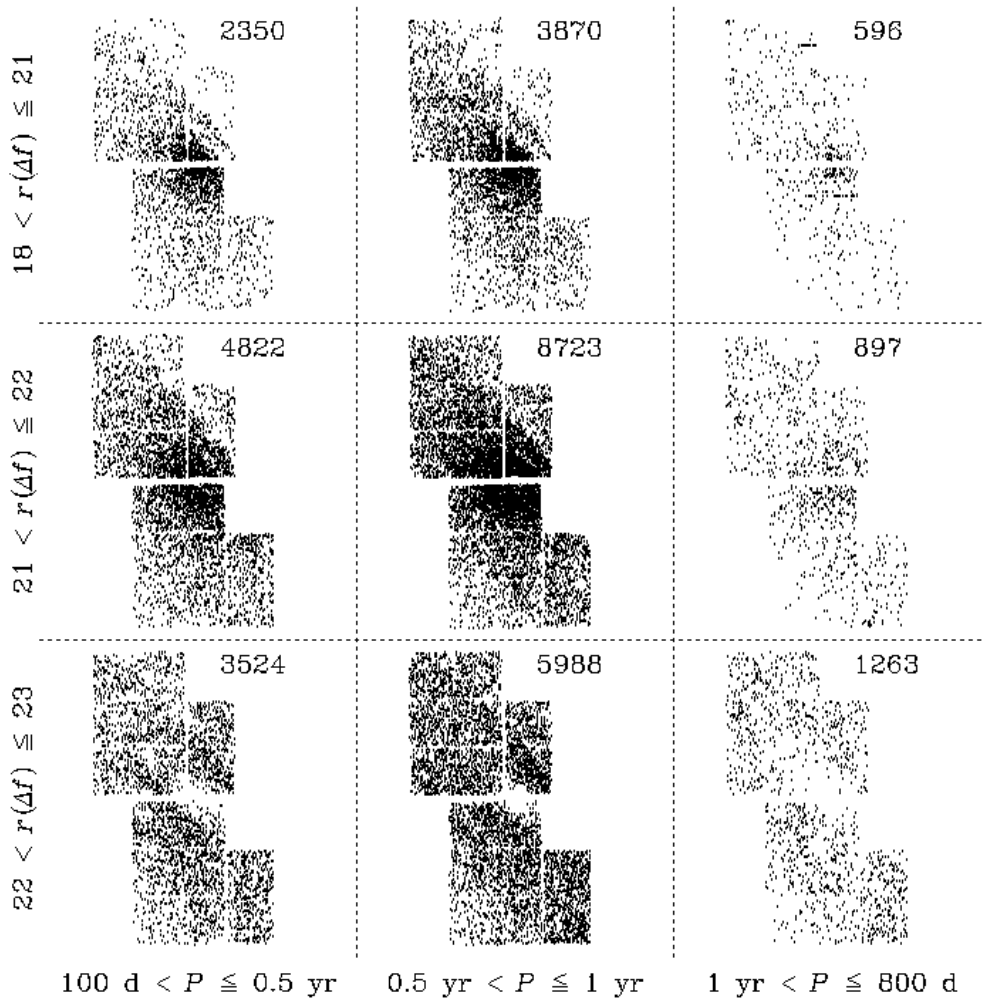


Figure 19. The spatial positions of all the variables in group 4 (primarily Miras and long-period variables), subdivided according to period and pseudo-magnitude. Note that there are obvious trends in that the brighter variables or ones with shorter periods are more centrally concentrated. The numbers of objects in each class are shown in the top-right hand corner of each sub-panel.

stars already seen in the lower three panels of Figure 3. This reinforces the identification of group 4 as predominantly semi-regular or Mira variables, as these correspond to pulsating AGB and RGB stars. One can discern a number of trends in Figure 19. First, for all but the faintest and longest period variables, there is an overall depression of objects in the north-west, which coincides with the prominent dust lane visible in the colour map of Figure 2. Second, the central concentration of objects varies noticeably, with the brighter (and probably shorter period) variables being more centrally concentrated. While the depression of detected variables with $r(\Delta f) > 22$ near the bulge is probably caused by the decline of detection efficiency due to high surface brightness, one can still observe the clear trend of a flattening in the number density gradient as the variation becomes fainter (and longer). This is also illustrated in Figure 20, which shows the logarithm of the surface density plotted against distance along the major axis for the subdivisions of group 4 variables. The period of a Mira is believed to be an indicator of the population to which it belongs (White-

lock 1996). Miras with periods less than 200 days are thought to be primarily denizens of the halo, whilst those of longer period are more massive and/or more metal-rich. The longer period Miras – being more massive and/or more metal-rich – are therefore associated with younger populations. In other words, the spatial distribution of the younger Miras is more extended than that of the older ones. The same conclusion can be drawn from the variation of central concentration according to the brightness. The AGB is redder and therefore optically fainter for a metal-rich population. This is consistent with the idea that the visually brighter Miras represent older populations. All this is consistent with the fact that the disk scalelength of M31 is larger in the blue than the red (e.g., Waltherbos & Kennicutt 1988). It is also consistent with a division of M31 stars into two populations, younger and bluer ones in the disk (Population I), older and redder ones in the bulge and spheroid (Population II), as discovered by Baade (1944).

We examine the distributions of variable stars broken down into different pseudo-magnitude and period bins. For comparison

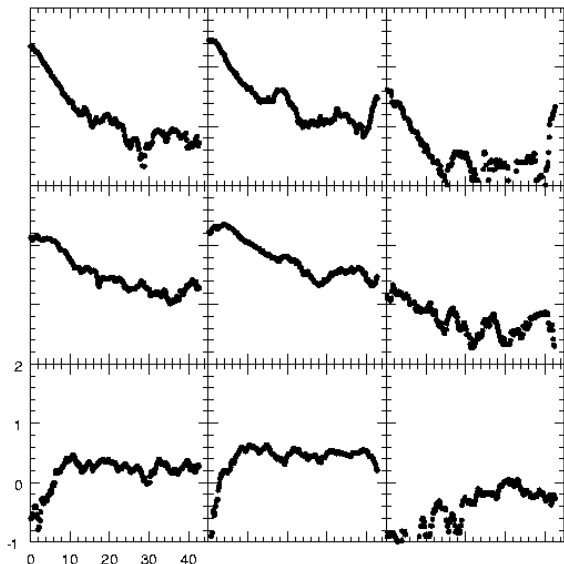


Figure 20. The logarithm of the surface density plotted against distance along the major axis towards the north-east for the classes of variable object in Figure 19.

purposes, this is done for the same symmetrically positioned fields as used for the resolved stars (N1, S1 and N2, S2 illustrated in the side-panel of Fig. 4). Figure 21 shows the numbers of variables with periods less than 800 days in each magnitude bin. By a slight abuse of terminology, we refer to these distributions as “luminosity functions”. For the exterior fields (N1 and S1), the luminosity functions are in good agreement for $r(\Delta f) < 22$. Note that, even up to $r(\Delta f) = 22$, the luminosity functions are still rising. This suggests that incompleteness in our variable star detection is not a substantial problem at least up to $r(\Delta f) = 22$ for these exterior fields. For the interior fields (N2 and S2), there is a difference in the overall normalisation causing the luminosity functions to be offset. This is most likely due to the dust lane in the N2 field. The luminosity functions for the interior fields rise more steeply than for the exterior fields. This is probably caused by underlying differences in the stellar populations, as the bulge contribution dominates in the interior fields. The luminosity functions for the interior fields also start to decline at $r(\Delta f) = 21.5$. This can be understood by the higher surface brightness in the bulge, which in turn means that the detection efficiency is lower. Figure 22 shows the numbers of variables with $18 < r(\Delta f) \leq 23$ as a function of the logarithm of the period. The bin size is 0.1 dex. For the exterior fields, there is a good agreement between the two distributions. The distribution is flat ($dn/dP \propto P^{-1}$) between periods of 1 and 40 days, reflecting predominantly the properties of the Cepheid population. Between 40 days and 0.5 yr, the population is made up mainly of semi-regular variables and Miras and the distribution is well-approximated by a power-law ($dn/dP \propto P$). The fall-off for longer periods may be caused by the decline in detection efficiency because of incomplete sampling. For the interior fields, there is a depression in the distribution derived for the N2 field as compared to the S2 around periods of 100 days. This in turn suggests that it is fewer objects with $P \sim 100$ days that are responsible for the smaller number of detected objects in the N2 field.

As for the resolved stars discussed in § 3, we construct smooth

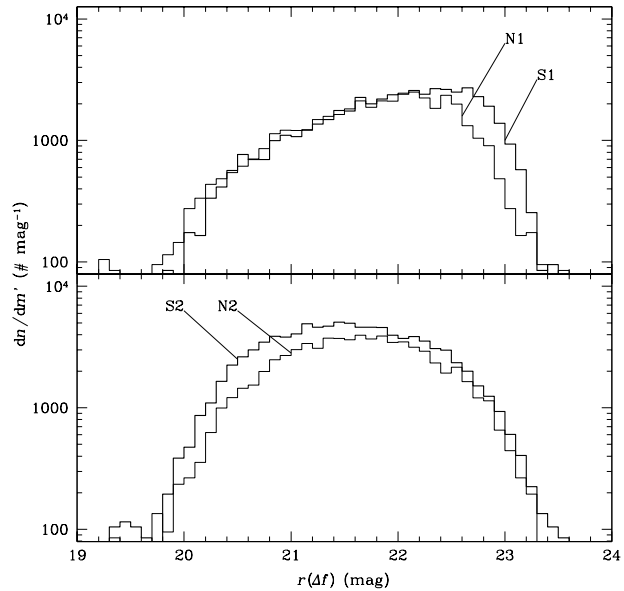


Figure 21. The observed uncorrected luminosity function for the variables stars in the same symmetrically positioned fields as Fig. 4. The bin size is 0.1 magnitudes. Only the variables with $P \leq 800$ days are included.

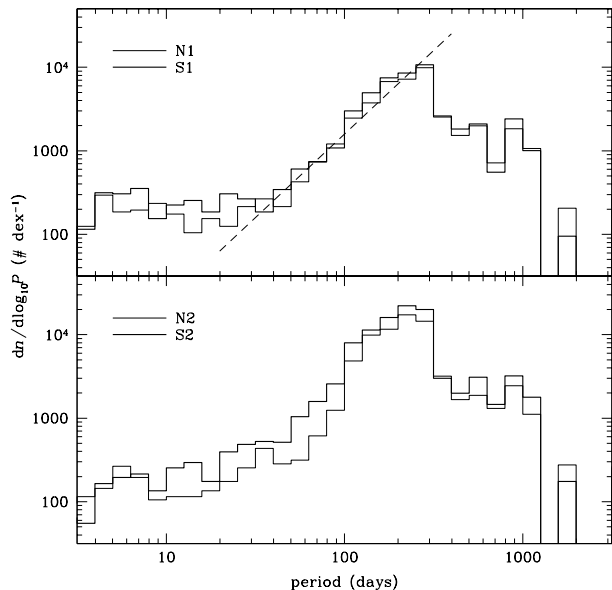


Figure 22. The period distribution of the variable stars in the same symmetrically positioned fields as Fig. 4. Only variables with $18 < r(\Delta f) \leq 23$ are included. The dashed lines has a slope of 2 and coincides with the rising part of the function in all four fields.

surface number density distributions of the variable stars. Here, we use a window function that is a square box of size $3'$. The result is compared with the surface brightness map and the resolved star ($R \leq 21$) density map in Figure 23. *None* of the three images show any sign of CCD to CCD or field to field overall scale variation. This is very reassuring as it suggests that our variable star detection is not systematically biased. Second, the resolved star distri-

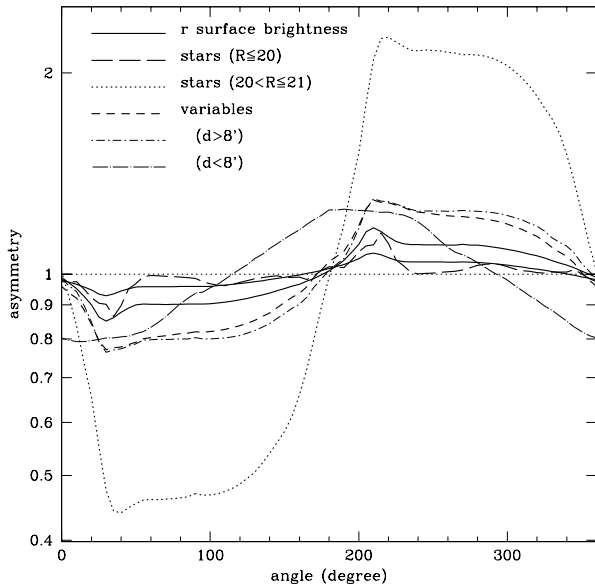


Figure 25. The ratio of the mean density on either side of an axis plotted against position angle of the axis for the brightest resolved stars (long dashed line), intermediate brightness resolved stars (dotted line), variable stars (short dashed line) and the integrated r band light (two solid lines – see text for difference). Also shown (the two dot-dashed lines) are the variables divided according to projected distance to the centre of M31.

bution shows a much more prominent ring-like structure (possibly just the spirality) than the variable star distribution. Third, the projected shape of the triaxial bulge is much less evident in the variable star map than in the other two maps.

6 THE ASYMMETRIES OF THE VARIABLE STARS

To examine the asymmetry of these distributions, we construct division images – that is, each image is divided by a copy of the image which is rotated by 180° with respect to the M31 centre. The resulting division maps are displayed in Figure 24. In all three cases, it is clear that the far side (south-east) is brighter or has more detected objects than the near side (north-west). More importantly, the asymmetry pattern of all three images quite closely follow each other, with the dust lane in the north-west clearly visible in all cases. It is therefore clear that a crucial assumption underpinning the microlensing experiments towards M31 – namely, that the variable star population is unlikely to show an asymmetry between the near and far side (Crotts 1992) – is unfortunately not correct. The intrinsic distributions are probably well-mixed, but the effects of differential extinction and the prominent dust lanes associated with the spiral structure in M31 cause all the observed distributions, whether of resolved stars or of variable stars, to be markedly asymmetric.

Any axis through the centre divides the galaxy into two parts. The ratio of the mean density on each side changes as the axis changes. We call the direction in which this ratio is maximised the asymmetry axis. To find the asymmetry axis, we construct the logarithm map of the division image and compute the ratio of the mean density of each side as a function of the position angle of the axis, measured anti-clockwise from north through east. The results are

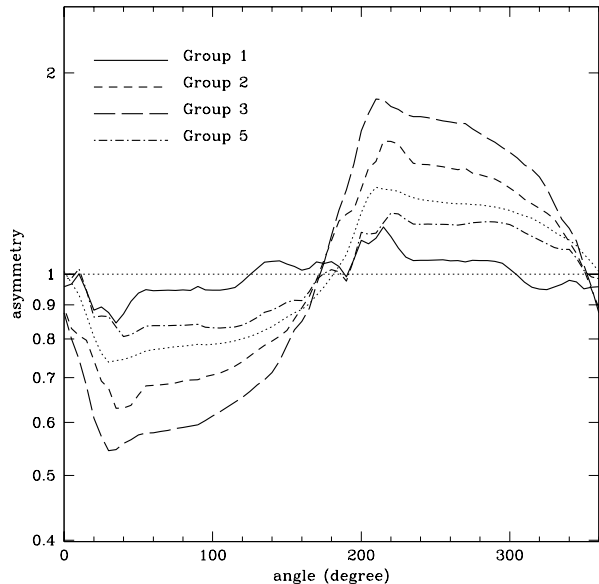


Figure 26. The asymmetry signal as a function of position angle for the variable stars in groups 1, 2, 3 and 5. The dotted curve shows the asymmetry signal of the 35414 variable stars in the catalogue. Both Fig. 26 and Fig. 27 are not corrected for the effects of M32 or HD 3914, but we have shown in the text that the correction is small.

shown in Figure 25. The long-dashed line is for the brightest resolved star ($R \leq 20$) density, while the dotted line is for the intermediate brightness resolved star ($20 < R \leq 21$) density. The two solid lines are derived from the r band image. The curve showing the larger asymmetry amplitude assumes the minimum contribution from the sky, while the smaller amplitude curve assumes the maximum contribution, and thus the reality should be somewhere in between. The maximum contribution is inferred from the reduced images without sky-subtraction, while the minimum contribution is derived from the south-east corner of field 2, CCD 1, which is assumed to contain no contribution from M31. Finally, the short-dashed line shows the asymmetry of the variables. This can be divided into the contributions from the bulge and disc respectively, by crudely dividing into two samples according to the projected distance d . The asymmetry of the whole variable sample follows that of the disc variables alone. This is because the asymmetry signal is weighted according to projected surface area, and so the effect of the bulge is minimal. Note that the contribution from M32 and a ~ 7 th magnitude star (HD 3914) lying just at the southern edge of the southern field CCD 2 is corrected for by excising a comparable area ($7' \times 7'$ mask) in both fields. In any case, their effects are minimal, again because they occupy very little of the total area.

The asymmetry of the brightest resolved stars – most likely young, massive supergiants – is virtually negligible. The asymmetry of the resolved stars with $20 < R \leq 21$ is quite noticeably enhanced compared to the total surface brightness. Some of this may be caused by the varying detection efficiency of the CCDs which is related to the choice of different reference images, as discussed in § 3. However, the fact that the pattern of the curve follows that for the surface brightness suggests that the effect is real, even if the magnitude is exaggerated. Such artificial enhancement is not expected for the variable stars, as the choice of reference image plays a less crucial role in the variable star detection algorithm. The re-

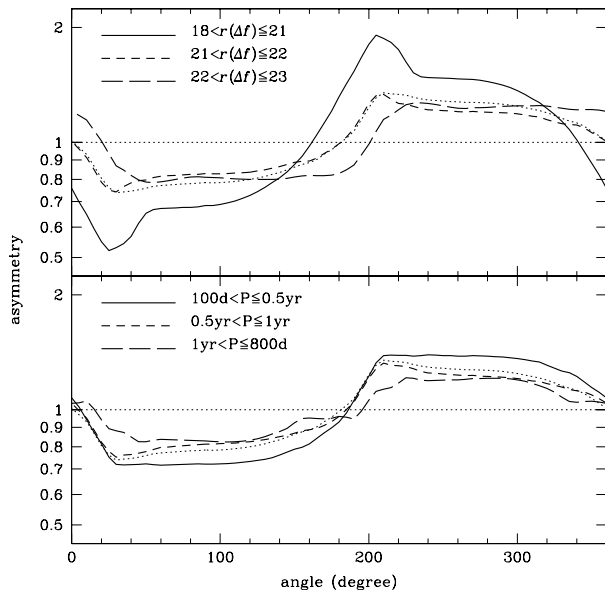


Figure 27. The asymmetry signal as a function of position angle for the variable stars in class 4, broken up according to pseudo-magnitude (top) and period (bottom). The criteria for the divisions of pseudo-magnitude and period are the same as recorded in Fig. 19. Also plotted in the dotted curve is the asymmetry signal of the 35414 variable stars in the catalogue.

solved stars are searched for on different reference images, which can have different photometric conditions, whereas the variables are searched for using the entire lightcurves and so the photometric conditions average out. In addition, both the magnitude of the asymmetry and the shape of the curve emphasise the fact that the variable star asymmetry is clearly associated with the underlying surface brightness. The maximum asymmetry occurs around $\sim 40^\circ$, while the symmetric division is around $\sim 180^\circ$, which is more or less an east/west division. For comparison, the position angle of the major axis of the outer disk is $\sim 38^\circ$ (de Vaucouleurs 1958), while the position angle of the bar is between 45° and 50° (Hodge & Kennicutt 1982). The fact that the maximum asymmetry occurs when the division lies almost parallel with the major axis provides further evidence that the asymmetry is mainly caused by the dust lane, as this too lies almost parallel with the major axis (see Fig. 2).

The asymmetry of the variable stars according to their group, period and pseudo-magnitude can be studied by exactly the same method. The results are shown in Figures 26 and 27. Since the effects of M32 and HD 3914 are not corrected for, the asymmetry is a bit larger than for the entire set of 35414 variables. We notice that the asymmetry signal of variables in group 1 (predominantly Population I Cepheids) is similar to that of the supergiant stars in Figure 25. Also, we deduce that the variable star asymmetry follows the asymmetry of the long period variables with $100 \text{ days} < P \leq 1 \text{ yr}$ and with $21 < r(\Delta f) \leq 22$. These are about $\sim 40\%$ of the variable star catalogue. There is a mild suggestion from the Figures that the asymmetry is larger for brighter variables, which is consistent with the enhanced asymmetry of the resolved star density between $20 < R \leq 21$. Probably both of these populations correspond to the brightest end of the AGB.

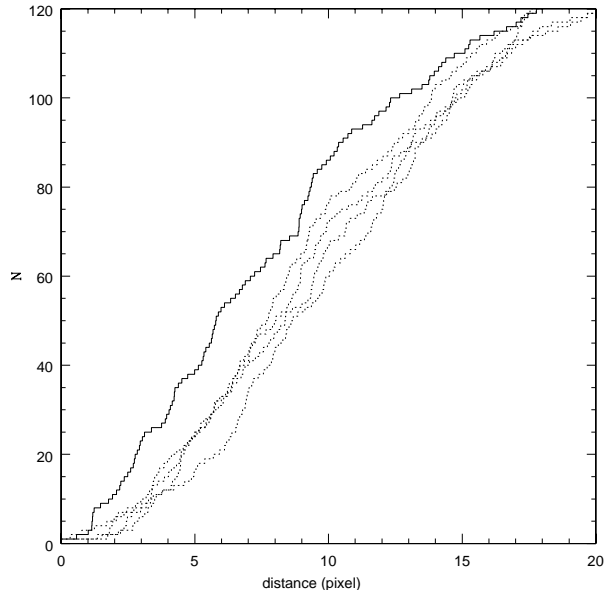


Figure 28. The full line shows the cumulative number of pairs matched between the optical and X-ray variable source catalogues as a function of separation. The dotted lines are constructed by first translating the optical catalogue by prescribed amounts in different directions and then correlating. So, this gives an idea of the number of accidental alignments expected.

7 CORRELATIONS WITH OTHER CATALOGUES

It is useful to compare our catalogue of variable stars with other surveys and archives of M31. Here, we correlate the catalogue with the discrete X-ray sources and the known novae.

7.1 X-ray Catalogues

M31 has recently been surveyed by both the XMM-Newton and Chandra satellites (Osborne et al. 2001; Kong et al. 2002). In particular, Chandra surveyed the inner $17' \times 17'$ and found 204 discrete X-ray sources. Our WFC fields are separated by a gap of $\sim 2'$, and so the very centre of M31 is not covered. This gap is rich in discrete X-ray sources, and so only ~ 140 of the objects listed in Kong et al. (2002) lie within our WFC fields.

Figure 28 correlates the variable sources in our catalogue with the discrete X-ray sources. To allow for possible identification with poorly sampled or sporadic optical sources, the primitive version of the catalogue with 97280 lightcurves is used. The figure shows the cumulative distribution of the separation distances. Of course, some accidental alignments are expected. To estimate how serious this problem is, we also show curves of the cumulative distributions with the optical positions shifted by 42 pixels north-east, north-west, south-east and south-west (Hornschemeier et al. 2001). This corresponds to a shift of 30 pixels in each compass direction. The claimed accuracy of the astrometry in both our and Kong et al.'s (2002) catalogue is $1''$. This suggests that objects can be identified if their positions coincide within an error circle of $1'4$ or ~ 5 pixels. Judging from Figure 28, the number of accidental alignments is ~ 25 , whereas the actual number of correlations is ~ 40 , which suggests that 15 ± 8 identifications are physically meaningful.

Some of the identifications are due to globular clusters. Whilst some of the globular clusters are indeed optically varying, the core

Table 2. Known novae detected in our catalogue. The number listed as the PA lightcurve refers to the number for the corresponding POINT-AGAPE superpixel lightcurve, which is also given in the subpanels in Fig. 30. For some cases, more than one nova-like superpixel lightcurve around a single nova position are detected as separate variable stars in our catalogue. However, all three cases of double detections show additionally variability in the baseline of the second lightcurve given in parentheses. The positions are directly measured from the resolved images of the novae near the maximum in the WFC *r* frames.

| Nova ^a | Alert | Position (J2000.0) | | PA lightcurve | Identifier ^b | Reference |
|--|----------------|--|------------|---------------|-------------------------|-----------|
| | | RA | Dec | | | |
| EQ J004249+411506 ^{c,d} | Jul 1999 | 00 ^h 42 ^m 49 ^s .7 | +41°15′08″ | 78668 | ... | 1 |
| EQ J004222+411323 ^e | Aug 1999 | 00 ^h 42 ^m 22 ^s .3 | +41°13′26″ | 83479 | ... | 2 |
| EQ J004241+411911 | Aug 1999 | 00 ^h 42 ^m 41 ^s .1 | +41°19′11″ | 25851 | PACN-99-05 | 3 |
| EQ J004244+411757 ^f | Jul 2000 | 00 ^h 42 ^m 44 ^s .0 | +41°17′57″ | 26946 | PACN-00-01 | 4 |
| EQ J004237.6+411737 | Aug 2000 | 00 ^h 42 ^m 37 ^s .7 | +41°17′39″ | 26021 (25568) | PACN-00-04 | 4 |
| EQ J004257+410715 | Oct 2000 | 00 ^h 42 ^m 57 ^s .1 | +41°07′17″ | 77716 | PACN-00-06 | 5 |
| EQ J0042.5+4114 ^d | Jul 2001 | 00 ^h 42 ^m 30 ^s .8 | +41°14′36″ | 81539 | PACN-01-01 | 6 |
| EQ J0042+4112 | Aug 2001 | 00 ^h 42 ^m 18 ^s .5 | +41°12′40″ | 83835 | PACN-01-02 | 7,8 |
| [OBT2001] 3 ^g | Sep 2001 | 00 ^h 42 ^m 34 ^s .6 | +41°18′13″ | 26277 (25695) | ... | 9 |
| EQ J004303.3+411211.3 | Oct 2001 | 00 ^h 43 ^m 03 ^s .3 | +41°12′12″ | 77324 | PACN-01-06 | 10 |
| EQ J004233+411823 ^h | Jan 2002 | 00 ^h 42 ^m 33 ^s .9 | +41°18′24″ | 26285 (26121) | ... | 11 |
| EQ J004252+411510 ^h | Jan 2002 | 00 ^h 42 ^m 52 ^s .9 | +41°15′11″ | 79136 | ... | 11 |
| ([?] CXOM31 J004318.5+410950) ⁱ | (Jul/Aug 2001) | 00 ^h 43 ^m 18 ^s .6 | +41°09′50″ | 74935 | ... | |

^a The name of the nova follows SIMBAD.

^b The identifier shows the label given by Darnley et al. (2004) to the nova.

^c The alert occurs before our first observation. However, the lightcurve shows the behaviour consistent with a fading nova. This is also studied in Riffeser et al. (2001).

^d The lightcurves are quite noisy.

^e [?] C84 25 / CXOM31 J004222.3+411333 / CXOM31 J004222.4+411334 (Kaaret 2002; Kong et al. 2002).

^f [?] CXOM31 J004243.9+411755 (Kaaret 2002).

^g [?] XMMU J004234.1+411808 / CXOM31 J004234.4+411809 (Osborne et al. 2001; Trudolyubov, Borozdin, & Priedhorsky 2001; Kong et al. 2002).

^h The alert occurs near the very end of our observation. Only sudden brightening at the end is observed in our lightcurves.

ⁱ We find the variable with a nova-like lightcurve within 0′.8 of CXOM31 J004318.5+410950 (Kaaret 2002). No alert for this nova has been reported during its outburst.

References. – (1) Modjaz & Li 1999; (2) Johnson, Modjaz, & Li 1999; (3) Li 1999; (4) Li, Papenkova, & Aazami 2000; (5) Donato et al. 2000; (6) Li 2001a; (7) Martin & Li 2001; (8) Aslan et al. 2002; (9) Fiaschi, di Mille, & Cariolato 2001; (10) Li 2001b; (11) Fiaschi et al. 2002.

of an unresolved globular cluster may also be misreported as a resolved star and this may cause spurious lightcurves in the catalogue. A handful of the identifications may be due to cataclysmic variables and soft X-ray transients. These are binary systems with a compact degenerate object and a low-mass star. Typically, they are undetectable in quiescence ($V = 28 - 30$) but brighten dramatically in outbursts ($V = 20 - 22$) and so may then be present in the survey.

Fourteen of the 40 correlations coincide with the positions of semi-regular variables, although for two of these instances, our sampling does not allow us to rule out the possibility of a bursting rather than pulsating star. Semi-regular variables are not expected to emit X-rays, unless they are the binary companion to a compact object. Hence, some of these alignments may well correspond to cataclysmic variables. Lightcurves for 6 of these objects are shown in Figure 29. We note that the lightcurves of r3-43 and r3-46 (in the notation of Kong et al. 2001) have an X-ray outburst ~ 50 days before the optical maximum. A further two objects, r3-87 and r3-48, coincide with optical variables showing a linear fall in the first two seasons. One of these is the lightcurve labelled 19755 shown in the top-left panel of Figure 14.

7.2 Nova Alerts

Nova alerts are published regularly in *IAU Circulars*. There are 14 nova alerts in M31 during the period that spans our WFC observations. We look for detections in our primitive variable star catalogue within a 3″ error circle of the reported nova position. This yields 12 matches to nova-like lightcurves. Both missing cases, EQ J004249+411632 (Filippenko et al. 1999) and EQ J004241+411624 (Fiaschi et al. 2002), lie very close to the centre of M31 and fall in the gap between the two fields. Table 2 gives the position, time of burst and reference of the 12 candidates, whilst the lightcurves are shown in Figure 30. All 12 detections are located within a few arcminutes of the centre of M31 and are either of fast or moderately fast speed class, presumably reflecting the experimental setup of the observers who issued the *IAU Circulars*. In addition, we find one further nova (CXOM31 J004318.4+410950) by correlating with the X-ray catalogue of Kaaret (2002). We note that another nova (EQ J004244+411757) also lies within 1′.3 of the position of an X-ray point source in the same catalogue. The X-ray counterparts of both novae have been claimed as super-soft X-ray sources by Di Stefano et al. (2003). A more detailed and homogeneous selection of novae using POINT-AGAPE data is performed in Darnley et al. (2004), who find 7 of the novae in Table 2. Darnley et al. (2004) also identify 13 other novae present in M31 further from the bulge and with longer durations and slower speed classes.

fig31.jpg

Figure 31. Locations of claimed microlensing events in M31, overplotted on the $g - r$ colour map. Circles show POINT-AGAPE candidates, crosses MEGA candidates and squares WeCAPP candidates. Also shown by a dot is the centre of M31, while the dashed line lies at position angle 38° (measured North through East) and marks the major axis of the outer disk.

8 DISCUSSION

Figure 31 shows the locations of 17 reported microlensing candidates (taken from Paulin-Henriksson et al. 2003, Riffeser et al. 2003 and de Jong et al. 2004) overplotted on the $g - r$ colour map. There is a clear asymmetry, as de Jong et al. point out. However, the origin of the asymmetry is difficult to say, as there are no events where the galaxy is dusty and a preponderance of events in the bright spiral arms. The early papers on microlensing towards M31 made the assumption that variable star populations would show no signs of asymmetry between fields north and south of the major axis. Microlensing, on the other hand, will show a substantial asymmetry if the lensing population resides in a spheroidal halo. Early on, it therefore seemed that an asymmetry in the locations of a sample of microlensing events would be enough to identify the lensing population conclusively with the dark halo of M31. The work in this paper has demonstrated that this is not the case. All the variable star distributions are asymmetric in the sense that the far side (or south-east) is brighter or has more detected objects than the near side (or north-west). This is caused primarily by the effects of variable extinction and the prominent dust lanes associated with the spiral structure. Therefore, the near-far asymmetry signal of microlensing is unfortunately mimicked in the variable star populations, in the underlying surface brightness and in the resolved star catalogue. This makes an accurate measurement of the asymmetry signal caused by microlensing more difficult. This paper has measured the size and direction of the asymmetry signal as a function of the period and pseudo-magnitude of the variable stars. These data form the zero-point of the asymmetry scale. Microlensing by a dark halo is a possible explanation if the sample of microlensing candidates of given amplitude and period is more asymmetric than the corresponding variable stars.

Theoretical calculations of the expected magnitude of the near-far asymmetry signal from microlensing (e.g., Kerins et al.

2001, 2003) assume that the source population shows no preference between the near and far side. However, as the resolved star distribution is also asymmetric, it is clear that this assumption is questionable as well. The source population for the identifiable microlensing events is typically bright (though unresolved) stars, and so it too is likely to be asymmetric. Hence, the magnitude of the near-far asymmetry signal as calculated theoretically needs to be amplified by an additional factor. The values of the asymmetry reported in Kerins et al. (2003) must now be taken as lower limits.

For a spherically symmetric halo, Kerins et al. (2003) found that the underlying pixel-lensing rate in the far-disk of M31 is already more than 5 times the rate of near-disk events. Clearly, a still more substantial asymmetry is expected when the effects reported in this paper are included. However, successful measurement of the component of any asymmetry signal caused by microlensing is now much more difficult. In principle, the additional effects can be modelled and corrected for, but in practice this will make the results less robust. One way to overcome the difficulties is to limit the study to microlensing events of sources only brighter than some fixed magnitude at baseline. Analysis of the microlensing asymmetry as a function of the source flux will however require a large sample of events with high signal-to-noise ratio.

Another way of overcoming the difficulties is to look for an east-west asymmetry rather than a near-far asymmetry. Both the resolved stars and the various groups of variables are more-or-less symmetric about an axis running north-south, as seen in Figures 25 and 26. So, this suggests that the underlying populations of variables are indeed well-mixed and that their asymmetry has a common origin in the dust distribution and possibly some intrinsic disk surface density asymmetry. If so, we can correct for it by choosing the north-south axis as our reference axis. Even though the east-west microlensing asymmetry is less than the near-far asymmetry in the absence of dust problems, it is still asymmetric, as the eastern side contains much of the far disk. This effect should be detectable in cases when the halos contains a high fraction of massive compact objects.

9 CONCLUSIONS

The POINT-AGAPE collaboration has constructed a catalogue of the locations, periods and brightness of 35414 variable stars in M31. This is a by-product of our microlensing search. The variable stars have been classed into four groups – roughly corresponding to population I and II Cepheids, semi-regular and Mira variables of short period and long period Miras. The spatial distribution of the variable stars shows a number of interesting trends. In particular, the brighter and shorter period Miras are more centrally concentrated than their fainter and longer period counterparts. This suggests that the younger populations of AGB stars are more extended than the older one. The variable star catalogue has been correlated with the X-ray point source catalogue available from surveys with the Chandra satellite. After taking into account accidental alignments, we find that there are ~ 15 physically meaningful identifications. This finding will lead to additional complications in the measurement of any asymmetry due to microlensing. In particular, it may be advantageous to look for an east-west asymmetry rather than a near-far asymmetry.

ACKNOWLEDGEMENTS

The data were taken through the Isaac Newton Group's Wide Field Camera Survey Programme. This research has made use of the SIMBAD database operated at Centre de Données astronomiques de Strasbourg, Strasbourg, France. We thank Albert K. H. Kong for providing us with the unpublished lightcurves of selected X-ray point sources in M31 and Vasily Belokurov for guidance on variable star catalogues. Work by JA and YT has been supported through a grant from the Leverhulme Trust Foundation. NWE thanks the Royal Society (UK) and the Particle Physics and Astronomy Research Council (UK) for support. SCN was supported by the Swiss National Science Foundation and by the Tomalla Foundation. AG was supported by grant AST 02-01266 from the National Science Foundation (US).

REFERENCES

- An J. H. et al., 2004, *ApJ*, 601, 845
 Ansari R. et al., 1999, *A&A*, 344, L49
 Aslan Z., Khamitov I., Parmaksizoglu M., Uluç K., 2002, *IAU Inf. Bull. on Var. Stars*, 5322, 1
 Aurière M. et al., 2001, *ApJ*, 553, L137
 Baade W., 1944, *ApJ*, 100, 137
 Baade W., Swope H. H., 1963, *AJ*, 68, 435
 Baade W., Swope H. H., 1965, *AJ*, 70, 212
 Baillon P., Bouquet A., Giraud-Héraud Y., Kaplan J., 1993, *A&A*, 277, 1
 Bellazzini M., Ferraro F. R., Pancino E., 2001, *ApJ*, 556, 635
 Bertin E., Arnouts S., 1996, *A&AS*, 117, 393
 Bonanos A. Z., Stanek K. Z., Sasselov D. D., Mochejska B. J., Macri L. M., Kaluzny J., 2003, *AJ*, 126, 175
 Burgos C., Wald-Doghradjian D., 2002, Internal Report PCC 0211S, Université Denis Diderot - Paris VII
 Calchi Novati S., Jetzer P., Scarpetta G., Giraud-Héraud Y., Kaplan J., Paulin-Henriksson S., Gould A., 2003, *A&A*, 405, 851
 Ciardullo R., Ford H., Jacoby G., 1983, *ApJ*, 272, 92
 Crots A. P. S., 1992, *ApJ*, 399, L43
 Darnley M. et al., 2004, *MNRAS*, submitted
 Di Stefano R. et al., 2003, *ApJ*, submitted (astro-ph/0306440)
 Donato L., Garzia S., Gonano V., Sostero G., Korlevic K., 2000, *IAU Circ.*, 7516R, 1
 de Jong J. T. A. et al., 2004, *A&A*, in press (astro-ph/0307072)
 de Vaucouleurs G., 1958, *ApJ*, 28, 465
 Feast M. W., 1996, in Sterken C., Jäschek C., ed., *Lightcurves of Variable Stars*. Cambridge Univ. Press, Cambridge, p. 91
 Feast M. W., Glass I. S., Whitelock P. A., Catchpole R. M., 1989, *MNRAS*, 241, 375
 Fiaschi M., di Mille F., Cariolato R., 2001, *IAU Circ.*, 7709, 3
 Fiaschi M., di Mille F., Cariolato R., Swift B., Li W. D., the LO-TOSS, *IAU Circ.*, 7794, 1
 Filippenko A. V., Chornock R. T., Coil A. L., Leonard D. C., Li W. D., 1999, *IAU Circ.*, 7271, 2
 Glass I. S., Evans T. L., 2003, *MNRAS*, 343, 67
 Hodge P., 1992, *The Andromeda Galaxy*. Kluwer Academic, Dordrecht
 Hodge P., Kennicutt R., 1982, *AJ*, 87, 264
 Holland S., 1998, *AJ*, 115, 1916
 Hornschemeier A. E. et al., 2001, *ApJ*, 554, 742
 Irwin M., Lewis J., 2001, *New Astron. Rev.*, 45, 105
 Johnson R., Modjaz M., Li W. D., 1999, *IAU Circ.*, 7236Q, 1
 Kaaret P., 2002, *ApJ*, 578, 114
 Kerins E. et al., 2001, *MNRAS*, 323, 13
 Kerins E. et al., 2003, *ApJ*, 598, 993
 Kiss L. L., Bedding, T. R., 2003, 343, 79
 Kong A. K. H., Garcia M. R., Primini F. A., Murray S. S., Di Stefano R., McClintock J. E., 2002, *ApJ*, 577, 738
 Li W. D., 1999, *IAU Circ.*, 7249R, 1
 Li W. D., 2001a, *IAU Circ.*, 7674, 2
 Li W. D., 2001b, *IAU Circ.*, 7729, 2
 Li W. D., Papenkova M., Aazami A. B., 2000, *IAU Circ.*, 7477R, 1
 Le Du Y., 2000, PhD thesis, Université Pierre et Marie Curie - Paris VI
 Margon B. et al., 2002, *AJ*, 124, 1651
 Martin P., Li W. D., 2001, *IAU Circ.*, 7684, 3
 Magnier E. A., Augusteijn T., Prins S., van Paradijs J., Lewin W. H. G., 1997, *A&AS*, 126, 401
 Melchior A.-L. et al., 1999, *A&AS*, 134, 377
 Mel'Nik A. M., Dambis A. K., Rastorguev A. S., 1999, *Astron. Lett.*, 25, 518
 Mochejska B. J., Macri L. M., Sasselov D. D., Stanek K. Z., 2000, *AJ*, 120, 810
 Modjaz M., Li W. D., 1999, *IAU Circ.*, 7218R, 1
 Noda S. et al., 2002, *MNRAS*, 330, 137
 Osborne J. P. et al., 2001, *A&A*, 378, 800
 Paulin-Henriksson S. et al., 2002, *ApJ*, 576, L121
 Paulin-Henriksson S. et al., 2003, *A&A*, 405, 15
 Riffeser A. et al., 2001, *A&A*, 379, 362
 Riffeser A., Fliri J., Bender R., Seitz S., Gössl C. A., 2003, *ApJ*, 599, L17
 Rosino L., 1973, *A&AS*, 9, 347
 Rosino L., Capaccioli M., D'Onofrio M., della Valle M., 1989, *AJ*, 97, 83
 Press W. H., Teukolsky, S. A., Vetterling, W. T., Flannery B. P., 1992, *Numerical Recipes in Fortran 77*, 2nd edn. Cambridge Univ. Press, Cambridge
 Stanek K. Z., Kaluzny J., Krockenberger M., Sasselov D. D., Tonry J. L., Mateo M., 1999, *AJ*, 117, 2810
 Stanek K. Z., Garnavich P. M., 1998, *ApJ*, 503, L131
 Szkody P. et al., 2003, *AJ*, 126, 1499
 Trudolyubov S. P., Borozdin K. N., Priedhorsky W. C., 2001, *ApJ*, 563, 119L
 Walterbos R. A. M., Kennicutt R. C., 1988, *A&A*, 198, 61
 Whitelock P. A., 1996, in Sterken C., Jäschek C., ed., *Lightcurves of Variable Stars*. Cambridge Univ. Press, Cambridge, p. 106
 Whitelock P., Marang F., Feast M., 2000, *MNRAS*, 319, 728

Figure 10. ([fig10.gif](#)) Lightcurves of variable stars in group 1, folded by their periods. For visual aid, two cycles are plotted. The superpixel flux in ADU s^{-1} is plotted against time in days. The number in the right-hand corner is the identifier in our catalogue. Lightcurve 29439 is most likely an eclipsing binary, whilst the remaining lightcurves are Population I Cepheids. Of these, 19897 and 20539 have the nearly symmetric shape associated with the first overtone, whilst the remainder are pulsating in the fundamental mode.

Figure 11. ([fig11.gif](#)) Folded lightcurves of variable stars in group 2.

Figure 12. ([fig12.gif](#)) Folded lightcurves of variable stars in group 3.

Figure 13. ([fig13.gif](#)) Folded lightcurves of variable stars in group 4.

Figure 14. ([fig14.gif](#)) Lightcurves of variable stars with ill-determined or incomplete period (group 5).

Figure 23. ([fig23.jpg](#)) Grey-scale surface density maps of the resolved stars with $R \leq 21$ (left) and variable stars (right), together with the surface brightness in the r band (centre). Notice the ring-like structure visible in the resolved star map.

Figure 24. ([fig24.jpg](#)) Grey-scale division maps of the resolved stars (left) and variable stars (right), together with the surface brightness (centre). The surface density is divided by its 180° rotated image to form the division map, so the map gives a direct measure of the asymmetry.

Figure 29. ([fig29.gif](#)) Optical lightcurves of the possible matches with discrete X-ray sources in Kong et al. (2001). The numbers in the top left of each panel refers to the possible match and the separation.

Figure 30. ([fig30.gif](#)) POINT-AGAPE lightcurves of known novae. The flux in ADU s^{-1} is plotted against time in $\text{JD}-2451000$. The number in the right-hand corner is the identifier in our catalogue, also listed in Table 2.

This figure "fig02.jpg" is available in "jpg" format from:

<http://arxiv.org/ps/astro-ph/0401374v2>

This figure "fig05.jpg" is available in "jpg" format from:

<http://arxiv.org/ps/astro-ph/0401374v2>

This figure "fig10.gif" is available in "gif" format from:

<http://arxiv.org/ps/astro-ph/0401374v2>

This figure "fig11.gif" is available in "gif" format from:

<http://arxiv.org/ps/astro-ph/0401374v2>

This figure "fig12.gif" is available in "gif" format from:

<http://arxiv.org/ps/astro-ph/0401374v2>

This figure "fig13.gif" is available in "gif" format from:

<http://arxiv.org/ps/astro-ph/0401374v2>

This figure "fig14.gif" is available in "gif" format from:

<http://arxiv.org/ps/astro-ph/0401374v2>

This figure "fig15.gif" is available in "gif" format from:

<http://arxiv.org/ps/astro-ph/0401374v2>

This figure "fig23.jpg" is available in "jpg" format from:

<http://arxiv.org/ps/astro-ph/0401374v2>

This figure "fig24.jpg" is available in "jpg" format from:

<http://arxiv.org/ps/astro-ph/0401374v2>

This figure "fig29.gif" is available in "gif" format from:

<http://arxiv.org/ps/astro-ph/0401374v2>

This figure "fig30.gif" is available in "gif" format from:

<http://arxiv.org/ps/astro-ph/0401374v2>

This figure "fig31.jpg" is available in "jpg" format from:

<http://arxiv.org/ps/astro-ph/0401374v2>